Bali, E., et al., 2020, Geothermal energy and ore-forming potential of 600 °C mid-ocean-ridge hydrothermal fluids: Geology, v. 48, https://doi.org/10.1130/G47791.1

Supplementary Materials for: Geothermal energy and ore forming potential of 600 °C mid-ocean ridge hydrothermal fluids

Enikő Bali*, László E. Aradi, Robert Zierenberg, Larryn W. Diamond, Thomas Pettke, Ábel Szabó, Guðmundur H. Guðfinnsson, Guðmundur Ó. Friðleifsson, Csaba Szabó.

Correspondence to: eniko@hi.is

This PDF file includes:

Supplement1 - Methods

1) Analytical methods:

Microthermometry

Microthermometric analyses were carried out using Linkam TMS600 and Linkam TS1500 heating stages at the Lithosphere Fluid Research Lab of the Faculty of Science at the Eötvös University, Budapest (ELTE LRG). Doubly polished mineral chips were heated at a rate of 10 °C/min to approximately 20 °C below the phase transformation temperatures, at which point the heating rate was changed to 5 °C/min. The precision of temperature readings of the TMS600 and TS1500 stages is 0.2 and 2 °C, respectively. Phase transformations were determined by changing the temperature at the rate of 1 °C/min 10 °C below to 10 °C above the phase transformation temperatures and repeating this procedure a few times for each FIA. With the exception of the dissolution of S4 in brine inclusions, the Linkam TMS600 heating stage was used. The high-temperature (TS1500) stage was used to observe the dissolution of S4 and the homogenization of brine inclusions. The heating rate during these experiments was the same as in the low-T experiments.

Raman spectroscopy

Raman spectroscopy analyses were done at the Research and Instrument Core Facility Center of the Faculty of Science at the Eötvös University, Budapest (ELTE FS-RICF), both at room temperature and during the heating experiments. During room-temperature analyses a 100x objective (NA=0.9) was used, whereas during high-temperature measurements we used a 50x objective lens (NA=0.5). Analyses were carried out with a Horiba LabRam HR800 instrument, applying a 532 nm (green) laser with maximum laser energy of 130 mW (~25 mW on the sample surface), 100 μm confocal pinhole, 600 to 1800 gratings. Analyses were run for 30 seconds with 2–3 repetitions. Gas and liquid components were analyzed with the maximum laser energy, whereas for mineral phases we reduced the laser power to ~2.5 mW on the sample surface with a filter, in order to avoid beam damage.

During the high-temperature analyses, spectra were collected 10 to 60 minutes after the target temperature was reached. This was especially important during the homogenization experiments with vapor-rich inclusions. For each vapor-rich inclusion, spectra were collected twice at 590 °C, first at 10 minutes after the target temperature was reached, and again after 50-

60 minutes. This was done to avoid the presence of any metastable liquid film remaining upon heating. No difference was observed between the spectra collected before and after the target temperature was reached.

Raman mapping was conducted in order to identify stretching bands of a given mineral with different orientations. Maps were collected at room temperature, using a 100 μm confocal hole, 600 grooves/mm optical gratings, and 6-10 × 10 s acquisition time. The investigated spectral range was between 110 cm^{-1} and 1900 cm^{-1} (i.e. the "fingerprint" region), and between 2800 and 4000 cm-1 (i.e.: the "OH" region). The spectral resolution of the measurements was 3.0 cm^{-1} at 1707.9 cm^{-1} and 2.4 cm^{-1} at 3642.2 cm^{-1} (defined as the measured full width at half maximum values of neon atomic emission lines). The Raman maps were processed using LabSpec 5.

Electron microprobe analyses

Electron microprobe analyses of silicate melt inclusions were carried out with a JEOL JXA-8230 SuperProbe at the Institute of Earth Sciences, University of Iceland. Operating conditions were: accelerating voltage of 15 kV, beam current of 5 nA, and a beam diameter of 4 to 7 μm, depending on melt inclusion size. Analyses were acquired with WDS spectrometry where Na was analyzed first to minimize the effect of Na migration caused by the electron beam. Natural and synthetic standards from Astimex Ltd and the Smithsonian Institute were used for calibration. Additionally, we used ATHO rhyolitic glass as a secondary standard. Cathodoluminescence (CL) imaging and trace element analyses in quartz were carried out with the same instrument. For CL imaging a beam current of 50 nA was used. Trace elements were analyzed with an accelerating voltage of 15 kV, a beam current of 100 nA and a beam diameter of 10 μm.

Focused Ion Beam Scanning Electron Microscopy with Energy Dispersive Spectrometry – slice-and-view (FIB-SEM-EDS)

The FIB-SEM-EDS analyses were acquired with a FEI Quanta 3D Dual Beam SEM at the Research and Instrument Core Facility of the Faculty of Science, Eötvös University, Budapest (ELTE FS-RICF). The EDS analyses and SEM imaging were done using 15-20 kV acceleration voltage and 23.7–480 pA beam current, depending on magnification. The surface above a selected fluid inclusion was coated by a ~1 μm thin platinum layer in order to protect the

inclusion from the high current of Ga^+ ions used for milling the three trenches around the inclusion. Low-current Ga^+ ions were used for slicing the inclusion; the distance between the slices was ~150 to 250 nm depending on the suspected size of the smallest solid phases within the inclusions previously identified by Raman measurements. High-resolution secondary electron (SE) and backscattered electron (BSE) images were taken of each newly exposed surface (slice) of the inclusion in order to calculate the exact volume proportions of the different phases. Exposed solid phases were identified using point, or area measurements with a high-resolution EDAX SDD (Silicon Drift Detector).

Laser-Ablation-Inductively Coupled Plasma-Mass Spectrometry (LA-ICP-MS)

LA-ICP-MS analyses were acquired with an Agilent 8800 ICP-MS equipped with a GeoLas-Pro 193 nm ArF Excimer laser system at the Institute of Geological Sciences, University of Bern. GSD-1G glass was used as the standard for the calibration of trace elements and Scapolite crystal (Sca-17) for the calibration of S, Cl, Br (Seo et al., 2011). Each standard was analyzed 3 times before and after a block of ~12 fluid inclusions and host minerals to allow for true-time drift correction. Standard measurements took ~30 seconds, and the background signal was collected for >50 seconds. The spot size was 44 μm for GSD1G and 60 μm for Sca17. The protocol of individual fluid inclusion measurement closely followed that reported in Pettke et al. (2012). Whenever possible, a stepwise increase of the beam size prior to breaching the inclusion was employed to reduce catastrophic ablation of quartz. The final beam size varied between 18 and 44 μm, depending on inclusion size, which was generally between 8 and 25 μm. In the case of a few deeper inclusions, active focusing of the laser beam was also applied. Host mineral signals prior to, and after the inclusion signal, were used for host mineral correction, and where no clean host interval could be obtained from these signals, a separate host mineral measurement was done next to the inclusion using a 44 μm beam. For quantification of brine inclusions, a salinity of 5 wt% NaCl was used for internal standardisation, based on FIB-SEM results (TableS2). For vapor-rich inclusions 0.5 wt% $NaCl_{equiv}$ was used, which was derived from thermodynamic data (Driesner, 2007) based on the results of the heating experiments. The SILLS software was used for data reduction (Guillong et al., 2008).

2) Determination of volume proportion of phases in vapor-rich and brine inclusions

Volume proportions of mineral phases in four brine inclusions were determined based on backscatter and secondary electron images collected during FIB-SEM analyses. Fluid inclusions were sliced in 150 or 200 nm steps and backscatter and secondary electron images were collected on each slice. In each inclusion, the step size was constant. Larger inclusions were sliced by using 200 nm steps. These images were processed (with various phases delineated and identified in each image) with the computer program ImageJ and volume proportions in each image were calculated. The final volume proportions in a single inclusion were derived based on 31 to 61 images, depending on the inclusion size. Along with estimated mineral densities (Table S2), these volume proportions were used for mass balance calculations to determine the chemical composition of brine inclusions. The derived NaCl contents were subsequently used as an internal standard for LA-ICP-MS analyses.

Volume proportion of liquid and vapor phases in vapor-rich inclusions were determined in a similar way based on photomicrographs of 12 vapor-rich inclusions.

Supplement2 - Materials

1) General description of core 11:

Core 11 of the IDDP-2 borehole was collected between 4634.2 and 4642.8 m depth with a recovery of 88% (Friðleifsson et al., 2020). The main rock type is metagabbro, which generally retains its original igneous texture (Fig. S1a), but which has been pervasively hydrothermally altered (Friðleifsson et al., 2020). For example, igneous clinopyroxene has been replaced by hornblende, secondary clinopyroxene, and orthopyroxene (enstatite component between 60 and 40 mol%). Plagioclase varies in composition from andesine to anorthite and appears dusty due to abundant vapor-rich fluid inclusions. Igneous titanomagnetite was replaced by an equigranular intergrowth of magnetite and ilmenite. Hydrothermal biotite is a minor alteration phase in most samples from Core 11 (Friðleifsson et al., 2020, Zierenberg et al. in press). Clinopyroxene–orthopyroxene and hornblende–plagioclase geothermometry suggests that most of the hydrothermal alteration occurred at temperatures between ~800 and 825 °C. Magnetite–ilmenite geothermometry indicates that this mineral pair continued to re-equilibrate to temperatures near the present-day temperature of ~600 °C before being quenched by the drilling fluid during core recovery (Zierenberg et al. in press).

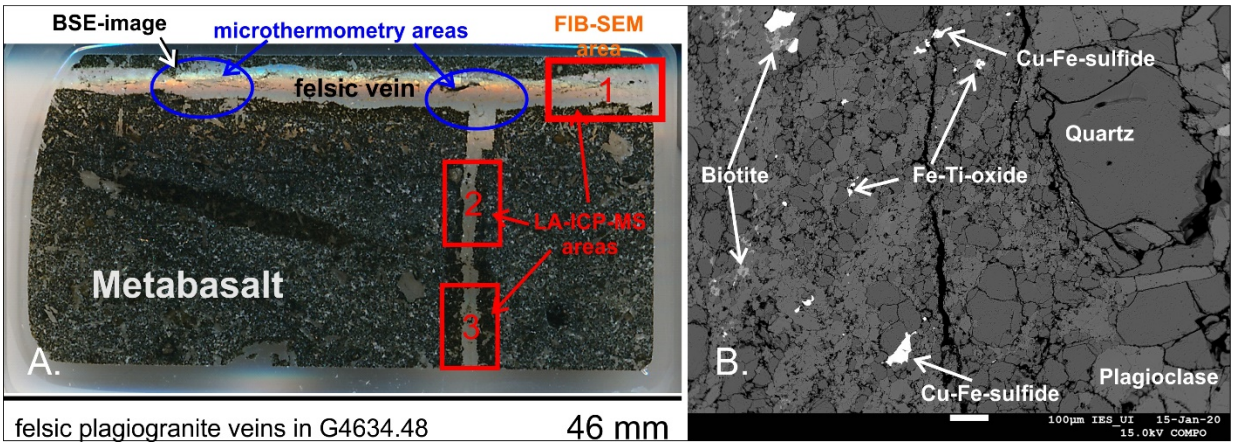

Fig. S1. A) Thin section of sample G4634.48 from the bottom of the IDDP-2 borehole, SW-Iceland. The picture shows the relationship between metabasalt and plagiogranite veins as well as the areas analyzed by different methods. Figure B is a Backscattered Electron (BSE) image of the same vein showing the main constituent minerals.

Plagiogranite veins are present in very minor abundance in metagabbro recovered below ~4300 m drilling depth. These veins are less than a few cm wide and formed as the last stage of igneous crystallization from a dacitic liquid. These veins are dominantly composed of intermediate plagioclase accompanied by minor quartz, apatite, biotite, titanomagnetite and trace euhedral zircon (Zierenberg et al. in press). Below ~4600 m drilling depth, the plagiogranite veins are generally much more quartz-rich (Fig. S1b) and rhyolitic in bulk composition, although show evidence of hydrothermal deposition of quartz and plagioclase, and in one vein, K-feldspar (Zierenberg et al. in press). Their trace element composition is markedly different compared to the dacitic veins, which are enriched in REE relative to the metabasalt, but have similar chondrite-normalized REE patterns that match the basalt. In contrast, these quartz-rich veins are strongly depleted in REE with a U-shaped REE pattern and a positive Eu anomaly (Zierenberg et al. in press). These trace element patterns match those of hydrothermal vein minerals from the shallower geothermal reservoir (Zierenberg et al. in press).

2) Petrography and composition of fluid and melt inclusions at room temperature

Based on petrographic observations, we have identified groups of coeval fluid inclusions (i.e., fluid inclusion assemblages, FIAs) in plagioclase and quartz of the plagiogranite veins. Inclusions trapped during growth of the host minerals, and hence during vein formation (i.e., primary inclusions), occur as FIAs along growth zones of individual crystals. In contrast, inclusions trapped after vein formation (i.e., secondary inclusions) are represented by FIAs within healed cracks (Fig. 2a) that cut grain boundaries. As secondary FIAs represent the modern deep geothermal fluid, this study focuses on their composition.

In order to confirm that these FIAs indeed cut grain boundaries and represent the latest fluid generation, we carried out cathodoluminescence (CL) imaging. The studied secondary FIAs are generally associated with “bright” fractures, which commonly connect to bright, fine-grained quartz along grain boundaries (Fig. 2a). Rarely, “dark” fractures cut these bright fracture zones. Although bright quartz (Fig. 2a) is more enriched in trace elements, including Ti (~200 ppm), compared to “dark” quartz (~100 ppm), this does not necessarily mean that these fractures represent higher T events. Trace element-rich quartz can also precipitate by rapid cooling (Huang and Audétat, 2012). Few fluid inclusions were analyzed in dark fractures too. No difference in chemical composition was observed compared to those in bright fractures. Therefore, we

concluded that the different quartz compositions related to different luminescence are the result of how fast the fractures healed rather than changes in temperature conditions.

Vapor-rich inclusions and are generally composed of a large dark vapor bubble and a thin liquid film around it (Fig. 2b, S2a, S3). In some of these inclusions, a small opaque phase can also be observed (Fig. S2a). At room temperature, the vapor phase in these inclusions is dominated by CO_2 with minor H_2S and traces of H_2 (Fig. S3; Table S3), whereas the liquid film is composed of low-salinity water (Fig. S4b, d). Based on the volume proportions of the liquid film and the vapor bubble in 12 inclusions at room temperature the density of the vapor-rich inclusions is estimated to be ~0.07 (±0.04) g/cm^3, assuming that the liquid phase at room temperature is pure H_2O. The density is likely to be higher due to the minor chloride component(s) (Table S1).

Brine inclusions are composed of four different solid phases, a vapor bubble ± a minor liquid phase (Fig. 2c, Fig. S2b, Fig. S5). The shape of the vapor bubble in these inclusions is always irregular, indicating that the liquid phase should be minor as the vapor largely fills the space remaining after the crystallization of the solid phases. Solid phase 1 (S1) is green to yellow pleochroic in plane-polarized light (Fig. S2b) and is strongly anisotropic, as seen with crossed polars (Fig. 2c). At room temperature this mineral has two characteristic Raman bands at 3451 and 200 cm^{-1} (Fig. S5b-d). Further smaller bands are observed in some of the spectra at 140 and 385 cm^{-1}. The approximate stoichiometry of this phase is $(Fe,Mn)_3(Na,K)_2Cl_3(OH)_5$ based on FIB-SEM-EDS analyses (Table S2). Solid phase 2 (S2) is also greenish in plane-polarized light (Fig 1c) and seems to be isotropic judging from observations made with crossed polars (Fig. S1b). This mineral has one characteristic Raman band measured at 3457 cm^{-1} (Fig. S3c) and its approximate stoichiometry is $(Fe,Mn)(Na,K)Cl(OH)_2$ (TableS2). The chemical composition and optical properties of this mineral are similar to douglasite (Palache et al., 1951). Solid phase 3 (S3) is a transparent, isotropic mineral (Fig 1c and Fig. S1b), commonly showing cubic crystal habit with no characteristic Raman bands and is a halite-sylvite solid solution dominated by the halite component (Table S1). Phase S4 (Fig 2c, Fig. S2b, Fig. S5) is a Cu-Fe sulfide (Table S1) with characteristic Raman bands at 381, 405 and 450 cm^{-1} (Fig. S5e), which are similar to those in molybdenite (Windom et al., 2011). Phases S1-S4 were observed by optical microscope in each brine inclusion and their phase transformations upon heating were easily recognized (see below). Based on FIB-SEM-EDS analyses, we identified further minor phases in these

inclusions, such as Fe-dominated chloride-hydroxide fluid condensate (similar in composition to akageneite), Ba-rich and Ca-rich chloride phases (TableS2), and apatite. The Fe-rich chloride-hydroxide fluid condensate commonly has a platy crystal habit in the opened inclusions, or coats the surfaces of other phases. When a fluid inclusion is opened during FIB-SEM analysis, a droplet of liquid escapes and after drying leaves behind material with this composition.

Silicate melt inclusions (Fig. 2d) are composed of a colorless silicate glass and a vapor bubble. The size of the vapor bubble is variable in these inclusions, and it is dominated by CO_2 and contains minor amount of H_2S. The bubble phase of these inclusions occasionally contains the S1 phase (Fig. S2e). Although melt inclusions are rare, it occurs in the secondary FIAs with vapor-rich and brine inclusions (FigS2c and d).

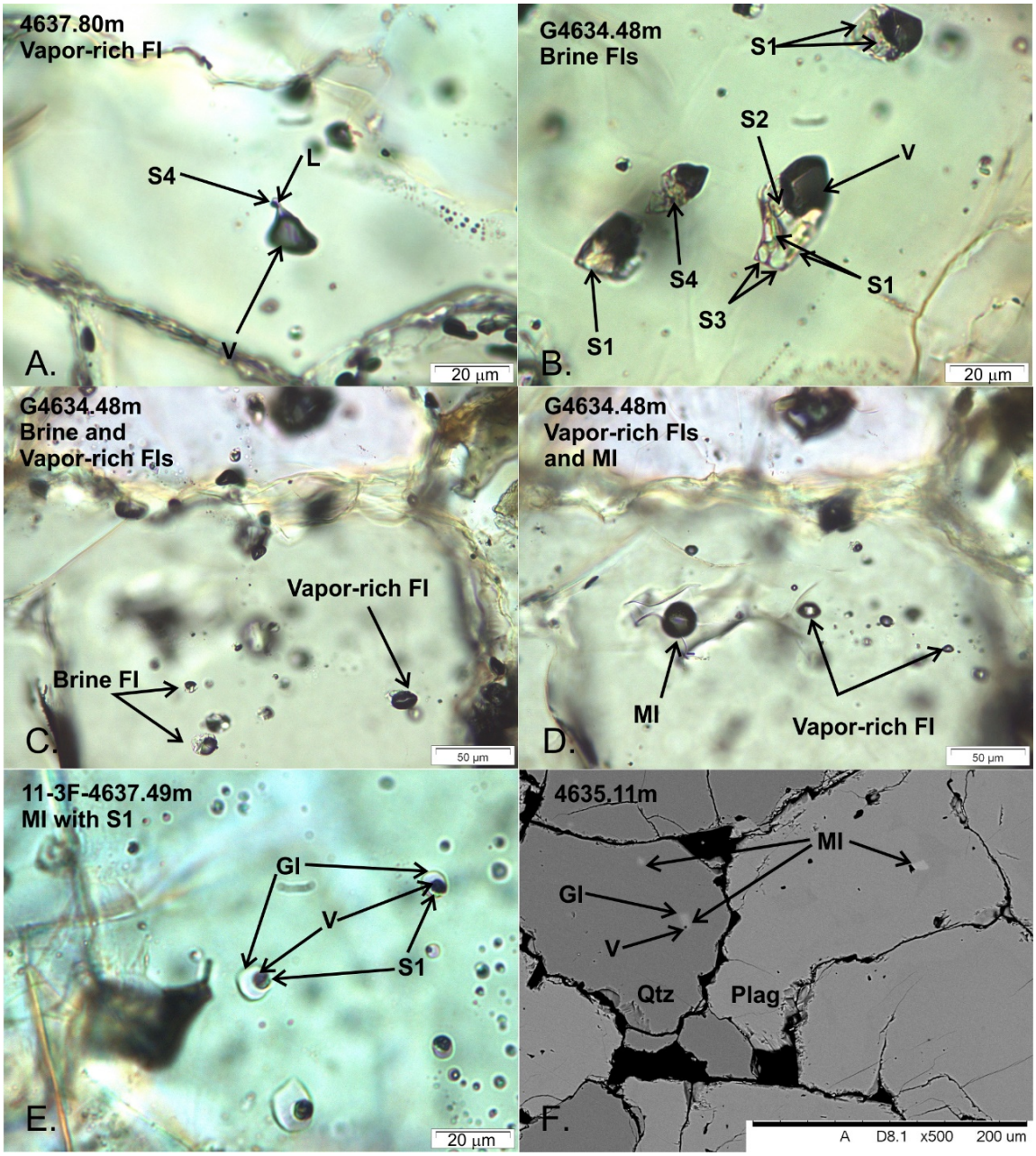

Fig. S2. Photomicrographs of the fluid inclusion assemblages (FIAs) from the bottom of the IDDP-2 borehole, SW -Iceland. A) Vapor-rich inclusion containing an opaque solid phase (S4). B) Brine inclusions with three of the four major solid phases (same as Fig. 2 but in plane-polarized light). C-D) Association of vapor-rich, brine and silicate melt inclusions within a single FIA; pictures are taken with the focus at different depths in the sample. E) Silicate melt inclusion with a vapor phase containing phase S1. F) Backscatter electron image of silicate melt inclusions in quartz (qtz) and plagioclase (plag). Pictures A-E were taken with plane polarized light. V – Vapor, L – Liquid, Gl – glass, FI – Fluid inclusion, MI – melt inclusion. Note that these images illustrate large inclusions to better visualize the different phases; most inclusions have sizes between 5 and 20 µm.

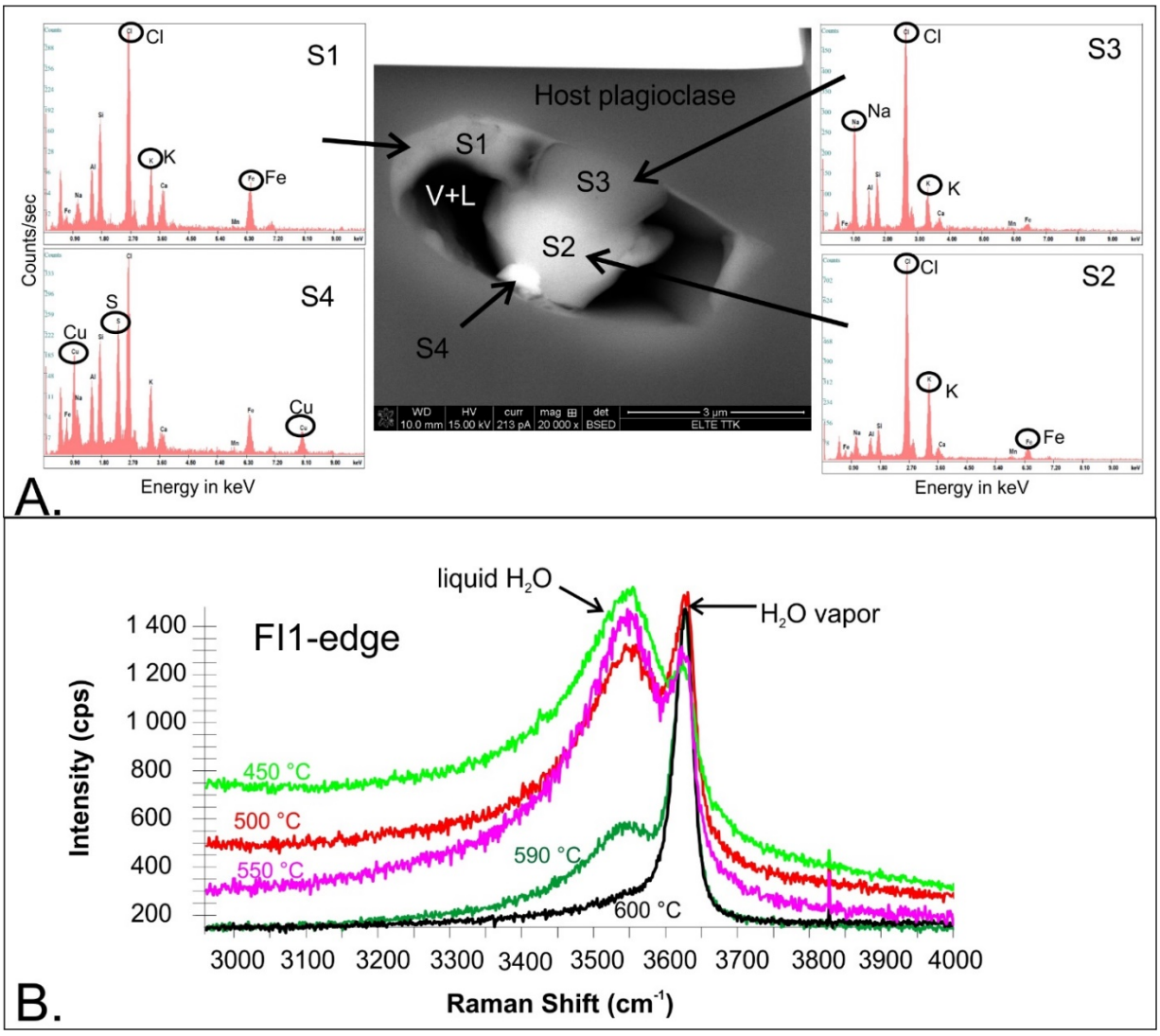

Fig. S3. Identity of phases in fluid inclusions from the bottom of the IDDP-2 borehole, SW Iceland. A) Backscatter electron image and energy dispersive spectra of mineral phases in brine inclusions as acquired by FIB-SEM-EDS (sample G4634.48m). This inclusion was analyzed in a plagioclase host. Therefore, the spectra include Si, Al and Ca peaks from the host owing to the somewhat larger excitation volume of the electron beam compared to the sizes of the solids in the inclusion. The Cl and K peaks in S4 are similarly the result of an overlap between S4 and S2. As the inclusion is breached, V+L is now a void previously filled by liquid and vapor. B) Raman spectra collected at the edges of the vapor-rich inclusion illustrated in Fig. 2b (sample 4637.80m) at temperatures between 450 and 600 °C in order to determine the temperature of complete

homogenization of the inclusion. Note that liquid H_2O (broad band at ~3540 cm^{-1}) was present up to 590 °C in each inclusion, even if the liquid film optically disappeared at 550 °C. Similar experiments were carried out on four additional vapor-rich inclusions, where the H_2O band also disappeared between 590 and 600 °C.

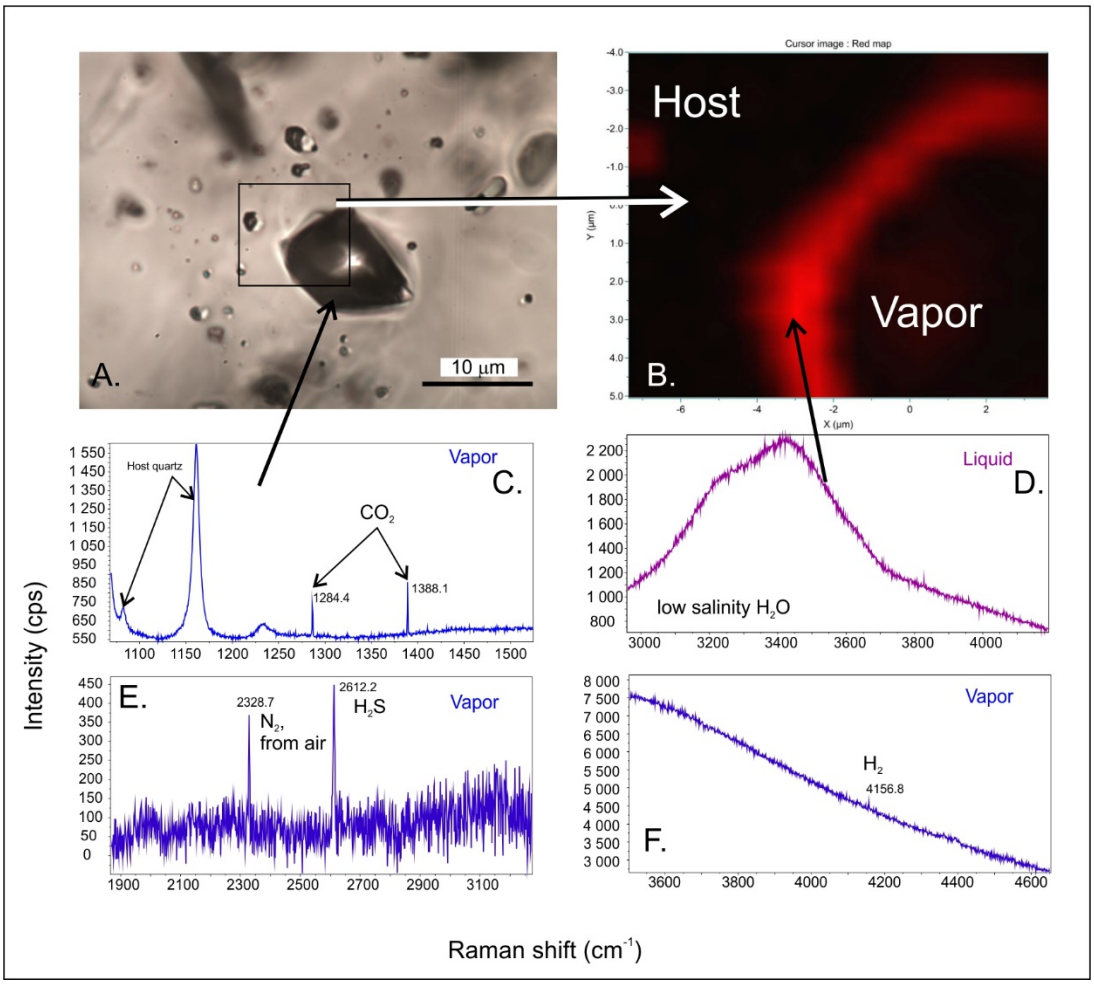

Fig. S4. Raman spectra of various phases in a vapor-rich inclusion from the bottom of the IDDP-2 borehole, SW Iceland. A) Photomicrograph of the inclusion taken with plane-polarized light. Box indicates the area of the Raman map in figure B. B) H_2O Raman map of the inclusion, where the red area indicates the H_2O-rich liquid film (spectrum D). The dark area is the host mineral and the vapor bubble (spectra C, E, F). All spectra were collected at room temperature. Sample N4635.25m.

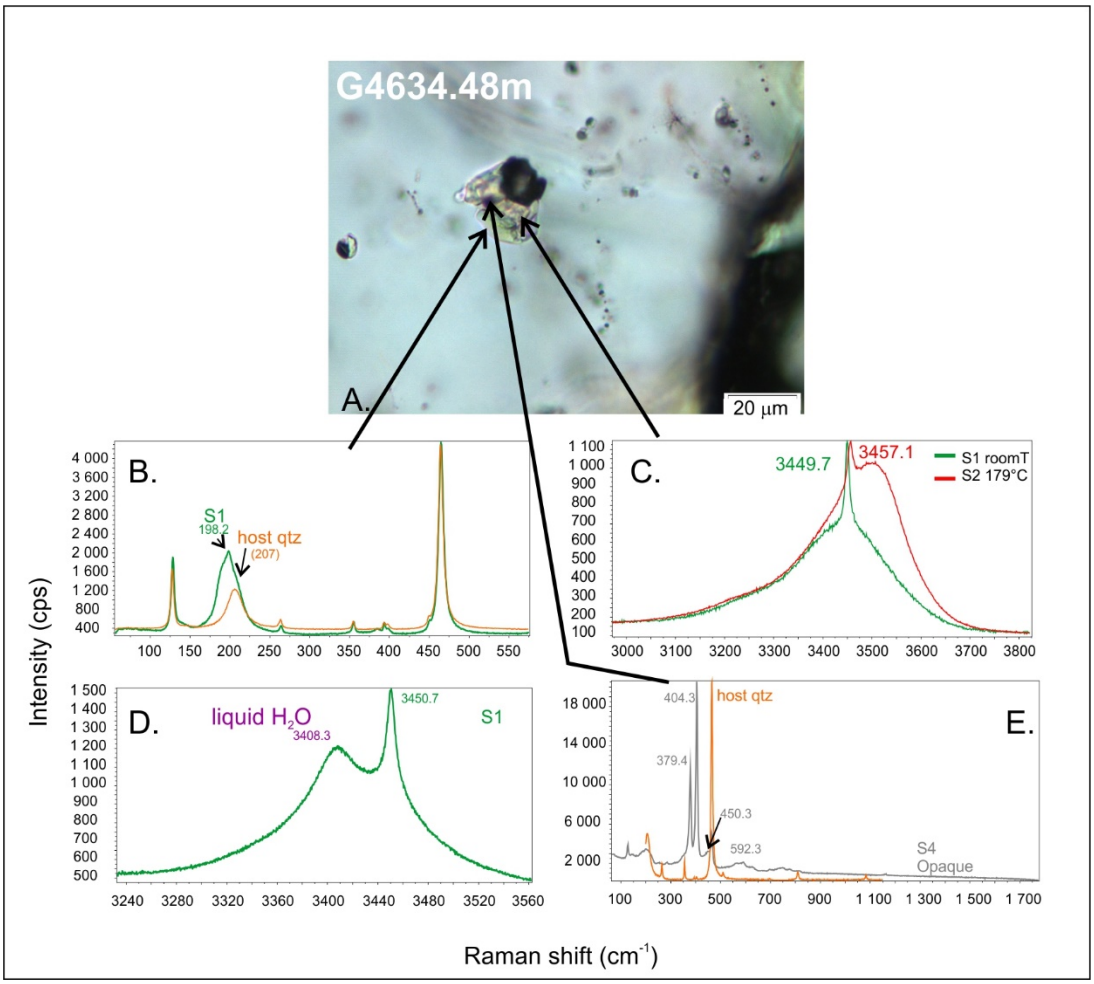

Fig. S5. Raman spectra of various phases in a brine inclusion from the bottom of the IDDP-2 borehole, SW Iceland (sample G4634.48m). A) Photomicrograph of the inclusion taken with plane-polarized light. Raman bands of S1 (B, C, D) are indicated in green compared to host quartz (B) and solid S2 (C); Raman bands of S4 (gray in e) compared to host quartz. All spectra were collected at room temperature, except that of S2 in Figure c, which was collected at 179 °C. The dissolution of S1, which commonly coats the surface of S2, at 179°C permitted analysis of pure S2 at high T.

Table S1. Average composition of vapor-rich and brine fluid inclusions from the IDDP-2 borehole below 4500 m depth. H_2O, CO_2, H_2S, and H_2 contents in vapor-rich inclusions were determined by Raman spectroscopy at 600 □C in homogenized inclusions. All other data are LA-ICP-MS results. Levels of detection (LODs) in µg/g report the numbers achieved during an ideal LA-ICP-MS measurement of an equant ~25µm brine inclusion (LODs for smaller inclusions are typically higher (see Pettke et al., 2012, for discussion). H_2 was not detected in the high-temperature Raman spectra; its abundance in the bulk fluid is calculated from its concentration in the bubble phase at room T (see Table S3).

	Mass measured	Vapor-rich (n=5)	2σ stdev(%)	Brine (n=30)	2σ stdev(%)	LOD in µg/g
H_2O	wt%	94.7	4	45.2	-	
CO_2		4.0	176	n.a.	-	
H_2S		1.3	114	n.a.	-	
H_2		b.d. (0.02*)	- (286)	n.a.	-	
		(n=4)				
Na	23	0.4	68	5	-	0.2
Cl	35	0.25	58	26.8	10	20
K	39	0.7	34	7.2	8.3	0.4
Ca	43	0.2	38	1.8	33	30
Mn	55	0.07	34	0.8	100	0.5
Fe	57	0.14	34	12.1	11	1.2
	µg/g					
S	34	200	134	1800	55	20
B	11	0.33	136	17	37	0.05
Mg	25	2.2	68	150	30	0.25
Cu	65	19	32	2000	30	0.02
Zn	66	24	40	2300	15	0.08
As	75	0.06	72	8.3	45	0.03
Br	79	21	20	1900	21	2
Rb	85	4.8	48	420	11	0.015
Sr	88	1.7	28	160	24	0.005
Mo	98	0.58	46	41	26	0.01
Ag	109	0.05	46	3.5	14	0.015
Cd	111	0.06	146	7.6	44	0.03
Sb	121	0.04	210	2.2	62	0.02
Cs	133	0.07	82	5.7	33	0.01
Ba	137	16	52	1300	26	0.02
W	182	0.19	50	16	37	0.01
Au	197	*<0.004*	-	0.14	70	0.008
Tl	205	0.01	66	1.2	31	0.01
Pb	208	0.54	48	41	40	0.008
Bi	209	0.01	58	1.2	38	0.005
Th	232	0.003	288	0.26	43	0.003
U	238	0.01	108	1.4	18	0.003

Table S2. Average composition of mineral phases and their volume proportions in brine fluid inclusions from the IDDP-2 borehole below 4500 m depth as determined by FIB-SEM-EDS. Compositions are in atomic % (at%) and weight % (wt%); variation is 1 σ standard deviation (stdev). Phases S7 and S8 were too small to analyze without contamination by the surrounding minerals. Thus, we report only the least contaminated analyses. Composition of S6 was observed in three fluid inclusions and probably represents mixed analyses of S1 and S2. Ss – solid solution, b.d. – below detection. OH was calculated based on charge balance.

Major phases distinguished by optical microscopy												
	S1, $(FeMnCa)_3(NaK)_2Cl_4(OH)_4$ n=24 in 4 FIs			**S2, $(FeMnCa)(NaK)_2Cl_3(OH)$ n=16 in 4 FIs**			**S3, Halite-Sylivite ss, n=13 in 4 FIs**			**S4, CuFe-sulfide, n=4 in 4FIs**		
	wt%	at%	stdev	wt%	at%	stdev	wt%	at%	stdev	wt%	at%	stdev
Na	0.9	1.4	1.0	3.0	4.7	2.0	22.1	31.2	7.2	-	-	-
Cl	30.3	29.5	6.1	43.9	44.7	3.6	63.2	58.5	9.0	-	-	-
K	16.3	14.4	3.9	23.9	22.0	2.6	5.1	4.3	2.9	-	-	-
Ca	1.7	1.5	1.5	1.0	0.9	1.2	0.9	0.8	0.5	-	-	-
Mn	2.2	1.4	0.8	3.4	2.3	0.4	1.0	0.6	0.4	-	-	-
Fe	33.0	20.4	3.0	18.6	12.0	1.6	8.0	4.7	2.6	28.4	25.8	3.1
Ba	b.d.	b.d.	-	b.d.	b.d.	-	b.d.	b.d.	-	-	-	-
S	b.d.	b.d.	-	b.d.	b.d.	-	b.d.	b.d.	-	25.3	38.5	5.3
Cu	b.d.	b.d.	-	b.d.	b.d.	-	b.d.	b.d.	-	46.2	35.7	5.2
OH	15.5	31.5	-	6.3	13.4	-	b.d.	b.d.	-	-	-	-
Vol%	12.9			7.9			10.0			0.8		
stdev	2.7			5.2			1.1			0.3		
density (g/cm3)	2.23			2.04			2.2			4.2		
Minor phases observed only during FIB-SEM analyses												
	S5, Fe-rich fluid condensate n=35 in 4 FIs			**"S6", S1-S2 ss or mix n=30 in 3 FIs**			**S7, Ca-rich chloride in 4 FIs**			**S8, Ba-rich chloride in 4 FIs**		
	wt%	at%	stdev	wt%	at%	stdev	wt%	at%		wt%	at%	
Na	1.3	2.0	2.3	0.9	1.4	1.8	0.5	0.8		0.8	2.4	
Cl	32.1	31.8	13.5	30.1	29.2	8.3	43.8	48.3		27.7	51.8	
K	6.5	5.9	13.4	21.4	18.8	5.7	4.5	4.5		2.6	4.4	
Ca	2.4	2.1	2.5	1.2	1.1	1.1	38.0	37.1		2.2	3.6	
Mn	2.0	1.3	0.9	2.1	1.3	1.3	b.d.	b.d.		-	-	
Fe	40.5	25.5	8.4	29.3	18.0	4.5	13.2	9.2		7.5	8.9	
Ba	b.d.	b.d.	-	b.d.	b.d.	-	b.d.	b.d.		59.1	28.5	
S	b.d.	b.d.	-	b.d.	b.d.	-	b.d.	b.d.		b.d.	b.d.	
Cu	b.d.	b.d.	-	b.d.	b.d.	-	b.d.	b.d.		b.d.	b.d.	
OH	15.2	31.5	-	15.0	30.3	-	-	-		-	-	
Vol%	8.4			9.3			0.5			0.4		
stdev	5.3			7.5			0.5			0.2		
density (g/cm3)	3.04			2.23			2.2			4.2		

Table S3. Compositions of vapor-rich and brine fluid inclusions, and of silicate melt inclusions from the IDDP-2 borehole, SW Iceland, below 4500 m depth. Analyses of vapor-rich inclusions were carried out using Raman microspectrometry at room temperature. Maximum and minimum solute contents in brine inclusions were determined by FIB-SEM (materials and methods). Major elements in melt inclusions were measured by electron microprobe.

Vapor-rich inclusions	**Vapor phase at room T**	**Liquid phase at room T**		
H_2O (mol%)	b.d.	100		
CO_2 (mol%)	77.9	b.d.		
H_2S (mol%)	16.5	b.d.		
H_2(mol%)	5.6	b.d.		
Brine inclusions	**Minimum solute concentration (wt%) FIB-SEM**	**Maximum solute concentration (wt%) FIB-SEM**	**Silicate melt inclusions**	**Average of 4 (1σ stdev)**
Na	3.7	5.1	**SiO_2**	77.9 (1.28)
Cl	26.9	37.0	**TiO_2**	0.07 (0.02)
K	9.3	12.8	**Al_2O_3**	10.2 (1.40)
Ca	1.6	2.1	**FeO**	0.50 (0.12)
Mn	1.4	1.9	**MnO**	0.02 (0.02)
Fe	18.6	25.7	**MgO**	0.04 (0.02)
Ba	0.5	0.7	**CaO**	0.93 (0.14)
S	0.5	0.6	**Na_2O**	2.44 (0.38)
Cu	0.9	1.2	**K_2O**	3.70 (0.63)
H_2O	36.7	12.7	**Cl**	0.27 (0.07)

Supplement3 - Results of fluid inclusion heating experiments

Microthermometric analyses were carried out on four samples (4635.11, A4637.80, N4635.25, G4634.48). In N4635.25, A4637.80 and G4634.48, we observed phase transformations and homogenization behavior of the brine inclusions, whereas in 4635.11 and G4634.48 phase transformations were observed in the vapor-rich inclusions. Some of these inclusions were also the subject to room-T and high-T Raman spectroscopy measurements.

Vapor-rich inclusions:

The reported observations are based on measurements carried out on two fluid inclusion assemblages (FIAs) in two samples that contained five fluid inclusions (three and two inclusions, respectively). While the vapor-rich inclusions were heated, the composition of the bubble phase as well as the liquid film (Fig. 1a2, FigS2) was monitored by Raman spectroscopy. In vapor-rich inclusions, the liquid film at the inclusion wall disappears optically upon heating at 550 °C. However, liquid H_2O is still detectable in the Raman spectra up to at least 590 °C at the margins of each studied inclusion (Fig. S3b). At 600 °C the liquid-H_2O signal disappeared in four out of five spectra, although in FI1 (Fig. S3b) there is a broad shoulder at the Raman shift of ~3540 cm^{-1} corresponding to liquid H_2O. Based on these observations, we conclude that vapor-rich inclusions homogenize into the vapor phase at 600±10 °C.

Brine inclusions:

The reported observations are based on measurements of seven fluid inclusion assemblages (FIAs) in four samples that contained 32 fluid inclusions in total. Phase transformations in brine inclusions were observed in the following sequence, upon heating: dissolution of the solid phases starts between 70 and 90 °C; S1 dissolves completely in each inclusion between 175 and 180 °C; S2 dissolves between 220 and 240°C; S3 dissolves at 377 to 390 °C; whereas S4 dissolves at 600±20 °C. At 600±20 °C, brine inclusions are composed dominantly of liquid hypersaline brine with minor, variable proportions of immiscible vapor. None of the brine inclusions homogenized completely below 715°C. It is also important to note that the dissolution of S4 was only observed in four brine inclusions. Although this phase was present in all brine inclusions, it was commonly attached to the dark bubble phase, which made clear observations of the disappearance of this phase difficult. We note that the dissolution of S3 in brine inclusions was

generally between 385 and 390 °C as determined by the Linkam TMS600 stage; lower temperatures were measured only during the high-T experiments carried out with the Linkam TS1500 stage.

The fact that the dissolution of S4 in brine inclusions and the evaporation of the liquid film in vapor-rich inclusions occur at the same temperature of 600±20 °C, we suggest that the trapping temperature of the endmember fluids to be close to this value at ~4500 m depth. Brine inclusions failed to homogenize completely to liquid at this temperature because they contain various amounts of accidently trapped vapor endmember. Thus, none of the analyzed brine inclusions are true endmember liquids.

Supplement4 – Magmatic fluid or modified seawater

We have the following arguments which suggests that the contribution of magmatic fluid to the hydrothermal fluid in this study is minimal.

1) The degassing of tholeiitic mid-oceanic ridge basalt (MORB) and its fractionation products produce magmatic fluids with low Cl/B ratios (Fig. S6 e.g., Arnórsson 1995, Aggarwal et al. 2000). This is because these melts are generally not saturated in chlorine due to their low original chlorine and H_2O contents.

We can demonstrate this by calculating boron and chlorine content of fluids (both vapor and brine) in equilibrium with average Mid Oceanic Ridge basalt (MORB) composition (Hart et al., 1999, Oppenheimer 2004) and with Icelandic rhyolite melt inclusions (Portnyagin et al., 2012 – the only available dataset with both B and Cl content for Hekla) (see figure below). Mixing of modified seawater with either a vapor or a brine phase degassing from MORB would decrease the Cl/B ratio in the hydrothermal fluid. This is true also for a degassing vapor phase from rhyolites. Indeed, low Cl/B values were measured in geothermal fluids sampled at Krafla (in 1979) during the Krafla fires as well as in the geothermal fluid in the IDDP-1 borehole which penetrated rhyolite magma body (see in figure below, and in Ármannsson et al., 2014). We do not see this decrease; in fact, the vapor phase has a similar Cl/B ratio to seawater, whereas some brine inclusions are slightly enriched in Cl relative to B instead of being depleted (probably due to phase separation between vapor and brine).

Degassing of a brine phase from Icelandic rhyolites might have Cl/B values close to that of seawater, but it has both Cl and B concentrations at least an order of magnitude lower than those observed in the brine inclusions in this study. I must emphasize, that for this calculation I used rhyolite melt inclusions from Hekla (as appropriate dataset is not available from other volcanic systems in Iceland). Hekla is a volcanic system characterized by transitional alkalic melts, and it is most probably enriched in both Cl and B relative to rhyolites from the main rift zone (where the Reykjanes Volcanic Belt is situated). Therefore, degassing brine or vapor might be poorer in both Cl and B in rift zone rhyolites than demonstrated here.

For comparison we plotted the composition of vent fluids sampled at Brothers volcano, (de Ronde et al. 2011). Cl/B values are distinct in those geothermal fluids suggesting the incorporation of magmatic fluid(s) to the hydrothermal system. This seems to be different in the Reykjanes deep fluids.

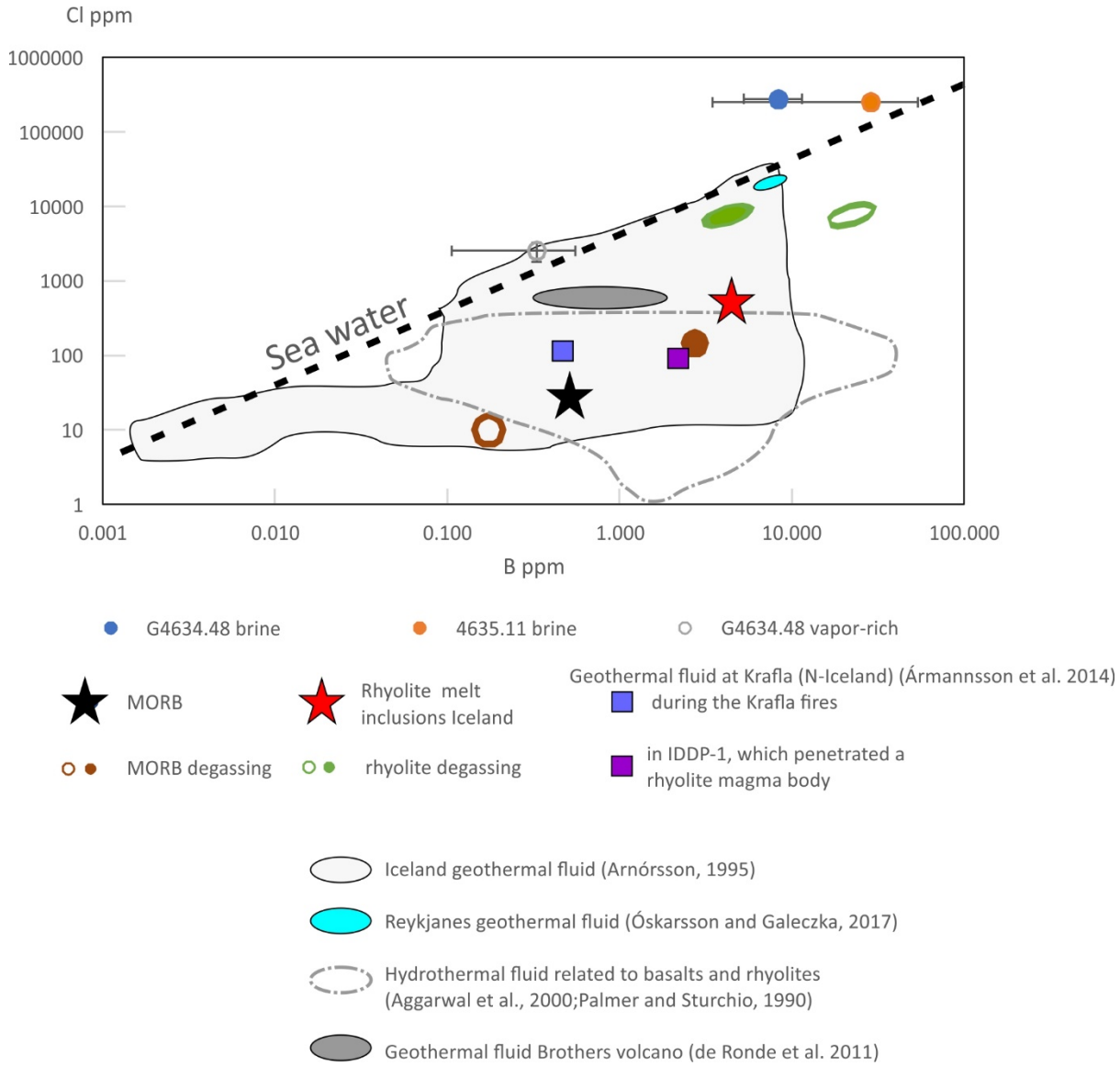

Fig. S6. Comparison of Cl and B contents of geothermal fluids from the IDDP-2 borehole to fluids derived by magmatic degassing. Partition coefficients for MORB and rhyolite degassing are from Hervig et al. (2002) (D_B in basalts), Mathez and Webster (2005) (D_{Cl} in basalt), Schatz et al., (2004) (D_B in rhyolite) and Doherty et al (2014) (D_{Cl} in rhyolite). Open circles – vapor phase, filled circles- brine phase. Data for Icelandic rhyolite is from Hekla melt inclusions of Portnyagin et al. (2012) MORB (Hart et al., 1999, Oppenheimer, 2004).

2) In tholeiitic systems the main degassing volatiles besides water are CO_2 and SO_2, which might contribute to the hydrothermal system above a shallow magmatic body. High pressure and temperature experiments demonstrated that from a basalt at shallow depths (100 to 300 MPa pressure) sulfur is preferentially released relative to chlorine and the S/Cl ratio in the degassing fluid is high (see e.g., Lesne et al. 2011). In accordance with this, significant sulfur release was observed during the last volcanic eruption of Iceland with only a minor outgassing of Cl (Gislason et al., 2015). The contribution of such fluid to the geothermal system was in fact observed in the IDDP-1 borehole at Krafla (N-Iceland), where a sulfur-rich, low-pH fluid cap was intersected before the drilling accidentally intersected a rhyolite magma body at ~2100 m depth (e.g.: Ármannsson et al. 2014). In the geothermal fluid, sampled at the well head in 2012, a S/Cl value of 0.1 was measured, whereas this ratio was 9.5 in geothermal fluids during the Krafla fires (see in: Ármannsson et al. 2014). If such fluid is incorporated in the hydrothermal system at Reykjanes, the S/Cl ratio in the hydrothermal fluid is expected to be above seawater values (0.047). In our inclusions, the S/Cl ratios are like that in seawater (or lower), thus no increase of S was observed. This does not exclude the addition of minor magmatic fluid to the system, but significant addition is not probable.

3) The enrichment of K over Na both in the brine and vapor excludes that these fluids are direct product of magmatic degassing. Tholeiitic basalts and their fractionation products are sodic, and in many cases contain only minor K_2O in Iceland. Experimental studies (e.g.: Clark, 1966, Ayers and Eggler, 1995) suggest that Na more readily partitions to a brine phase compared to K. Therefore, a tholeiitic melt with Na/K mass ratios above 1 cannot produce a degassing brine with Na/K mass ratios below 1.

Additional References:

Aggarwal, J.K., Palmer, M.R., Bullen, T.D., Arnórsson, S., and Ragnarsdóttir, K.V., 2000, The boron isotope systematics of Icelandic geothermal waters: 1. Meteoric water charged systems, Geochimica et Cosmochimica Acta, v. 64, p. 579-585.

Ayers, J.C., and Eggler, D.H. 1995, Partitioning of elements between silicate melt and H,O-NaCI fluids at 1.5 and 2.0 GPa pressure: Implications for mantle metasomatism: Geochimica et Cosmochimica Acta, v. 59, p. 4237-4246.

de Ronde,C.E.J., Massoth, G.J., Butterfield, D.A., Christenson, B.W., Ishibashi, J., Ditchburn, R.G., Hannington, M.D., Brathwaite, R.L., Lupton, J.E., Kamenetsky, V.S., Graham, I.J., Zellmer, G.F., Dziak, R.P., Embley, R.W., Dekov, V.M., Munnik, F., Lahr, J., Evans L.J. and Takai, K., 2011, Submarine hydrothermal activity and gold-rich mineralization at Brothers Volcano, Kermadec Arc, New Zealand: Mineralium Deposita, v. 46, p. 541-584.

Doherty A.L., Webster, J.D., Goldoff, B.A. and Piccoli, P.M., 2014, Partitioning behavior of chlorine and fluorine in felsic melt–fluid(s)–apatite systems at 50 MPa and 850–950 °C: Chemical Geology, v. 384, p. 94-111.

Gíslason, S.R., Stefánsdóttir, G., Pfeffer, M.A., Barsotti, S., Jóhannsson, Th. Galeczka, I., Bali, E., Sigmarsson, O., Stefánsson, A., Keller, N.S., Sigurdsson, Á., Bergsson, B., Galle, B., Jacobo, V.C., Arellano, S., Aiuppa, A., Jónasdóttir, E.B., Eiríksdóttir, E.S., Jakobsson, S., Guðfinnsson, G.H., Halldórsson, S.A., Gunnarsson, H., Haddadi, B., Jónsdóttir, I., Thordarson, Th., Riishuus, M., Högnadóttir, Th., Dürig, T., Pedersen, G.B.M., Höskuldsson, Á. and Gudmundsson, M.T. 2015, Environmental pressure from the 2014–15 eruption of Bárðarbunga volcano, Iceland: Geochemical Perspectives Letters, v. 1, p. 84-93.

Guillong, M., Meier, D.L., Allan, M.M., Heinrich, C.A., Yardley, B.W.D., 2008, SILLS: a MATLAB-based program for the reduction of laser ablation ICP-MS data of homogeneous materials and inclusions: Mineralogical Association of Canada Short Course, v.40, p. 328-333. with explanatory notes.

Hart, S.R., Blusztajn, J., Dick, H.J.B., Meyer, P.S. and Muehlenbachs, K. 1999, The fingerprint of seawater circulation in a 500-meter section of ocean crust gabbros: Geochimica et Cosmochimica Acta, v. 63, p. 4059-4080.

Hervig, R.L., Moore, G.M., Williams, L.B., Peacock, S.M., Holloway, J.R., Roggensack, K. 2002, Isotopic and elemental partitioning of boron between hydrous fluid and silicate melt: American Mineralogist, v. 87/5-6, p. 769-774.

Huang, R., and Audétat, A., 2012. The titanium-in-quartz (TitaniQ) thermobarometer: a critical examination and re-calibration: Geochimica et Cosmochimica Acta, v. 84,p. 75–89.

Mathez E.A. and Webster, J.D. 2005, Partitioning behavior of chlorine and fluorine in the system apatite-silicate melt-fluid: Geochimica et Cosmochimica Acta, v. 69, p. 1275-1286.

Oppenheimer, C. 2004, Volcanic Degassing. In: Treatise on Geochemistry. Holland, H.D. and Turekian, K.K. (Editors), Elsevier, Amsterdam, v. 3, p. 123-166.

Palache, C., Berman, H., and Frondel, C., 1951, Dana's system of mineralogy, (7th edition), v. II, p. 100. (http://webmineral.com/data/Douglasite.shtml#.XjhGUGj7Q2w).

Palmer M.R. and Sturchio N.C., 1990, The boron isotope systematics of the Yellowstone National Park (Wyoming) hydrothermal system: a reconnaissance: Geochimica et Cosmochimica Acta, v. 54, p. 2811–2815.

Portnyagin, M., Hoernle, K., Storm, S., Mirnov, N., van den Bogaard, C. and Botcharnikov, R., 2012, H2O-rich melt inclusions in fayalitic olivine from Hekla volcano: Implications for phase relationships in silicic systems and driving forces of explosive volcanism on Iceland: Earth and Planetary Science Letters, v. 357-358, p. 337-345.

Schatz O.J., Dolejs, D., Stix, J., Williams-Jones, A.E. and Layne, G.D. 2004, Partitioning of boron among melt, brine and vapor in the system haplogranite–H2O–NaCl at 800 □C and 100 MPa: Chemical Geology, v. 210, p. 135-174.

Seo, J.H., Guillong, M., Aerts, M., Zajacz, Z., and Heinrich, C.A., 2011, Microanalysis of S, Cl, and Br in fluid inclusions by LA–ICP-MS: Chemical Geology, v. 284/1–2, p. 35-44.

Windom, B.C., Sawyer, W.G., and Hahn, D.W., 2011, A Raman Spectroscopic Study of MoS2 and MoO3: Applications to Tribological Systems: Tribology Letters, v. 42/3, p. 301-310.